The 2018 Palu Tsunami: Coeval Landslide and Coseismic Sources

Amy L. Williamson[*1], Diego Melgar[1], Xiaohua Xu[2], and Christopher Milliner[3]

Abstract

On 28 September 2018, Indonesia was struck by an M_W 7.5 strike-slip earthquake. An unexpected tsunami followed, inundating nearby coastlines leading to extensive damage. Given the traditionally non-tsunamigenic mechanism, it is important to ascertain if the source of the tsunami is indeed from coseismic deformation, or something else, such as shaking induced landsliding. Here we determine the leading cause of the tsunami is a complex combination of both. We constrain the coseismic slip from the earthquake using static offsets from geodetic observations and validate the resultant "coseismic-only" tsunami to observations from tide gauge and survey data. This model alone, although fitting some localized run-up measurements, overall fails to reproduce both the timing and scale of the tsunami. We also model coastal collapses identified through rapidly acquired satellite imagery and video footage as well as explore the possibility of submarine landsliding using tsunami raytracing. The tsunami model results from the landslide sources, in conjunction with the coseismic-generated tsunami, show a greatly improved fit to both tide gauge and field survey data. Our results highlight a case of a damaging tsunami the source of which is a complex mix of coseismic deformation and landsliding. Tsunamis of this nature are difficult to provide warning for and are underrepresented in regional tsunami hazard analysis.

Introduction

Most tsunamis are generated from slip on faults, often associated with subduction zones. Such is the case for many destructive events of the past century, including the 2004 Sumatra, 2010 Maule, and 2011 Tohoku-Oki earthquakes. These large tsunamis typically exceed run-up heights of 10 m (Mori et al., 2011). Occasionally, earthquakes with a strike-slip mechanism will also generate tsunamis, albeit typically on a smaller scale. The 1994 Mindoro Island strike-slip earthquake in the Philippines caused measurable (3–4 m) run-ups near the source (Imamura et al., 1995). More recently, the 2010 Haiti earthquake generated a 3 m tsunami. Its complex source was a combination of coastal slumping and deformation related to strike-slip motion (Hornbach et al., 2010). The Palu earthquake, with a similar strike-slip mechanism, ruptured within the Indonesian island of Sulawesi. A portion of the rupture occurred in the narrow Palu Bay, where at its inland terminus, is the city of Palu with a population of over 300,000. It is within this bay where a damaging tsunami occurred. Surveyed run-ups reach 8 m with a maximum inundation distance of 430 m (National Geophysical Data Center [NGDC], 2018). Over 2200 casualties were reported related to the earthquake, tsunami, and landslides.

The Palu earthquake ruptured in part on the Palu-Koro fault, in a complex tectonic environment (Socquet et al., 2006).

The centroid moment tensor (U.S. Geological Survey [USGS], 2018) suggests a left-lateral rupture with a lesser component of normal faulting. This mechanism is consistent with long-term regional strain rate models and tectonic studies (Walpersdorf et al., 1998; Bellier et al., 2001; Socquet et al., 2006; Watkinson and Hall, 2017). Although the fault trace of the Palu-Koro fault as well as some secondary local transpressional faults have been mapped, the fault structure through the bay, where the rupture has its tsunamigenic potential, is poorly constrained.

The tsunami is surprisingly large for the associated earthquake magnitude and faulting mechanism. Because of this anomalous behavior, various aspects of the earthquake and tsunami source have garnered attention and an extensive scientific discussion has formed over the exact tsunami source mechanism. Complicating analysis, direct observations of the tsunami are limited to only one tide gauge within the bay, eyewitness accounts, and limited video recordings. In the months following the earthquake, numerous post-event field surveys have been conducted, providing insight into the inundation,

1. Department of Earth Sciences, University of Oregon, Eugene, Oregon, U.S.A.;
2. Scripps Institutions of Oceanography, University of California San Diego, La Jolla, California, U.S.A.; 3. Jet Propulsion Laboratory, California Institute of Technology, Pasadena, California, U.S.A.

*Corresponding author: awillia5@uoregon.edu

run-up, and damage from the tsunami (see Omira *et al.*, 2019; Paulik *et al.*, 2019; Putra *et al.*, 2019).

With this data in hand, various studies have provided compelling arguments for components of the event. For example, modeling of hypothetical landslides sources was carried out by Heidarzadeh *et al.* (2019) and incorporated in Pakoksung *et al.* (2019), advocating that the dominant landslide that caused the tsunami recorded at the tide gauge was submarine and generated near the entrance of the bay to the northwest. Takagi *et al.* (2019) focused on one particular subaerial landsliding event near Palu City (southwest of the Pakoksung *et al.*'s model) and how it affected inundation in its immediate surroundings, omitting any coseismic effects from the earthquake. Frederik *et al.* (2019) published post-event bathymetric survey results for non-coastal (>50 m water depth) parts of Palu Bay, identifying regions that potentially slumped based on the gradient at the expected scarp locations. Sassa and Takagawa (2019) and Arikawa *et al.* (2018) identified features through field surveys that may have contributed to tsunami waves during the earthquake. Each study provides valuable insight into possible landsliding processes or mechanisms. Focusing instead on the earthquake, additional recent studies have advocated for a tsunami generated purely through coseismic deformation, without invoking landsliding as a tsunamigenic mechanism. Song *et al.* (2019), for instance, model the event through two rupturing fault segments, deriving a fault model through ascending and descending radar data. Ulrich *et al.* (2019) also advocate for a coseismic only source model based on a teleseismically validated dynamic rupture scenario.

To date, however, a unifying tsunami model that simultaneously fits the field-survey measurements, the tide gauge amplitude, and the timing of the main tsunami arrival, while also being accurate in modeling the earthquake rupture, has not yet been accomplished. The missing link is a model that is self-consistent with the on-shore geodetic data that govern the earthquake rupture as well as the field survey and tide gauge data that govern the tsunamigenic behavior over the entire bay. In this study, we posit that *all* of these mechanisms, subaerial and submarine landslides, and coseismic offsets contribute to the tsunami's damaging impact. We explore many possible tsunami sources in addition to the earthquake's rupture near the bay, solving for both coseismic offsets and potential landsliding events in a self-consistent model. First, we focus on the coseismic component of the earthquake, solving for the distributed slip using crustal offset data. Because of ambiguities in the rupture as it transects the bay, we test three different fault geometries. We compute the resultant tsunami for each of the fault models, initially ignoring any effects related to landsliding, and compare with tsunami observations. This provides a baseline coseismic tsunami component that is then included in landslide-centric models.

Next, we identify potential landsliding events along the coast of Palu Bay. Using satellite imagery from the days following the event, we identify the locations and coastal area lost due to mass wasting and test the tsunami run-up potential for all sources. We compare these landsliding events in addition to our best coseismic model to the same field and tide-gauge observation data as our previous coseismic-only model. The final component of this study is an assessment of potential additional submarine mass wasting sources that would not be apparent on post-event satellite imagery. We outline the locations within Palu Bay that, based on travel time, are most favorable to contribute to the tsunami, as decided by misfits in run-up and tide gauge data and guided through tsunami raytracing. These locations are then modeled and discussed in the context of bathymetric surveys conducted following the earthquake. Our results lead us to conclude that coseismic deformation does contribute to tsunamigenesis; however, subaerial and submarine landsliding are crucial to correctly approximating tide gauge and run-up observations.

Data
Geodetic
To constrain the coseismic component of slip that may contribute to the tsunami, we acquired line-of-sight (LoS) crustal deformation using a pair of ascending images from Advanced Land Observation Satellite-2 operated by the Japanese Aerospace Exploration Agency (JAXA). The first satellite pass was collected on 17 August 2018 and the second pass was on 12 October 2018. The interferometric synthetic aperture radar (InSAR) data were processed using the GMTSAR (Sandwell *et al.*, 2011) software with outcoming phase unwrapped (SNAPHU) using statistical-cost, network-flow algorithm for phase unwrapping (Chen and Zebker, 2013). The postprocessing was done with Generic Mapping Tools (Wessel *et al.*, 2013). The resultant image provides good coverage over the entire Palu Bay region; however, some on-land areas immediately adjacent to the inferred fault trace are decorrelated. We subsampled the LoS image over the entire model domain, ignoring the offshore and decorrelated masked regions (Fig. S1, available in the supplemental material to this article). Our spatial sample rate was every 2 arcmin in the north–south and east–west directions. This amounts to 631 sample points that were used in the inversion. The maximum deformation in the positive LoS (toward the satellite) direction occurs northwest of Palu Bay (Fig. 1). The maximum deformation in the negative LoS (away from satellite) direction occurs in the sediment basin immediately south of Palu City proper.

In supplement to the InSAR data set, we incorporate subpixel correlation of optical images acquired before and after the earthquake from the Sentinel-2 and Planet labs sensors (Planet Team, 2018) (Table 1). We used an image correlation method (Debella-Gilo and Kääb, 2011) applied to the visible bands, which calculates the normalized cross-correlation between the images and achieves subpixel precision by interpolating for the correlation peak. To resolve the deformation field to the same scale given the Sentinel-2 and Planet labs imagery have different image
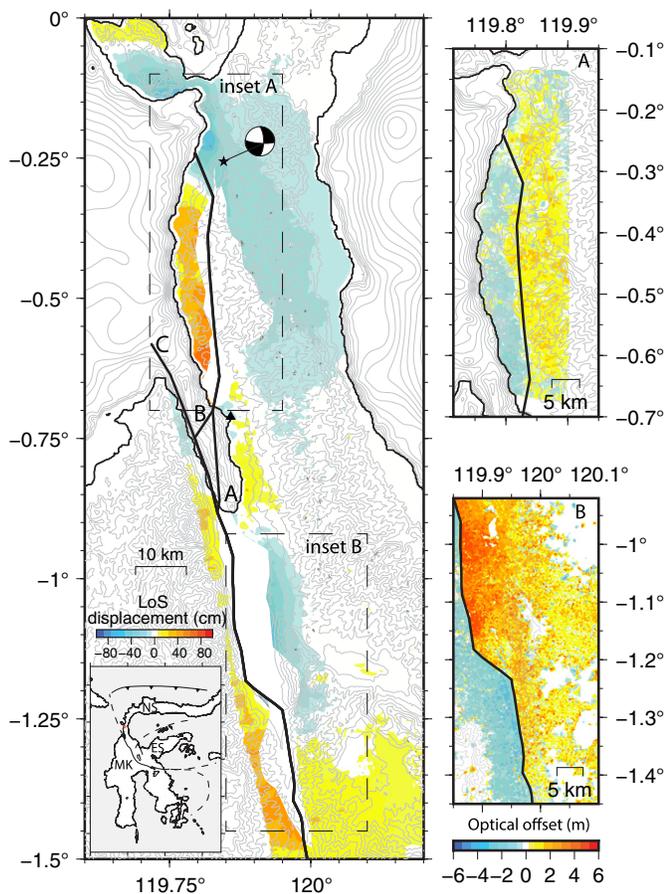
Figure 1. Static offsets following the Palu earthquake in central Sulawesi. Main figure: unwrapped surface deformation in the line-of-sight (LoS) direction. Star indicates the U.S. Geological Survey (USGS) determined epicenter with corresponding moment tensor. Thick black lines indicate the fault trace for the three potential fault models labeled A, B, and C. Black triangle indicates Pantoloan tide gauge. Inset map shows regional view of Sulawesi, including principle faults and the presence of three microblocks (MK, Makassar; NS, North Sula; and ES, East Sula) as discussed in Socquet *et al.* (2006). Insets A and B show optical offsets in the north–south direction. Note a change in color scale between optical and LoS data sets. The color version of this figure is available only in the electronic edition.

resolutions (10 and 3 m, respectively), we used correlation windows with step sizes of 9 and 30 pixels, respectively, resulting in a correlation map of 90 m pixel resolution. Areas of decorrelation are caused primarily by the presence of clouds. However, these occur mostly away from the surface rupture allowing assessment of near-field surface motion. The inclusion of 2D horizontal offset data provides key offset information near the fault trace, where the InSAR data set is decorrelated.

Tsunami

Geodetic data can be used to identify deformation on land; however, it is largely insensitive to submarine deformation.

TABLE 1
Timing Information for the Optical Image Correlation Analysis

Sensor	Pre-event (yyyy/mm/dd)	Post-event (yyyy/mm/dd)
Sentinel-2	2018/03/20	2018/10/25
Planet labs	2018/09/27	2018/10/02

To validate tsunami models, tide gauge and field survey data are necessary. The tsunami was recorded at the Pantoloan tide gauge northeast of Palu City (Fig. 2). Although the sample rate of the gauge is relatively slow, 1 sample per minute, it is the only tide gauge available within Palu Bay. Although coarse, the waveform exhibits two important characteristics that a model should be able to recover. First, the tsunami did not arrive immediately after the onset of the event; the first large arrival takes place at 5 min after the earthquake origin time. Second, the initial dominant signal was a negative wave followed by a near equally large crest. The measured amplitude from trough to crest is 4 m, with the caveat that due to the gauge sample rate, the amplitude may be underreported. The arrival time is a strong constraint on the location of the tsunami source and the large amplitude provides information on the expected scale of the tsunami's source. Furthermore, the tide gauge observation is consistent with collocated and time-tagged video footage of the tsunami's arrival near Pantoloan (see Carvajal *et al.*, 2019).

Numerous post-event field studies have been published, identifying the extent of damage, tsunami inundation, and run-up (Paulik *et al.*, 2019; Putra *et al.*, 2019; Syamsidik *et al.*, 2019). We compare our results with run-up heights measured by multiple post-event field campaigns (Mikami *et al.*, 2019; Omira *et al.*, 2019; Widiyanto *et al.*, 2019). One of the earliest studies, focusing within the bay (Omira *et al.*, 2019), measured run-up heights at 19 locations in exceedance of 4 m (Fig. 2). The coastline immediately northwest of Palu City, near the terminus of Palu Bay, experienced run-ups exceeding 6 m. Near the entrance to and outside of Palu Bay, there are fewer survey measurements, but run-up heights are lower with one surveyed location measuring 0.9 m. Further to the northeast, no tsunami damage was observed (Omira *et al.*, 2019). We use our tsunami model fits to both the tide gauge time series and this run-up data to evaluate each of our earthquake source models.

Methods
Fault geometry
The geometry of the fault within the bay dictates the location of tsunamigenic seafloor deformation, which in turn can affect tsunami modeling results. The path of the Palu-Koro fault
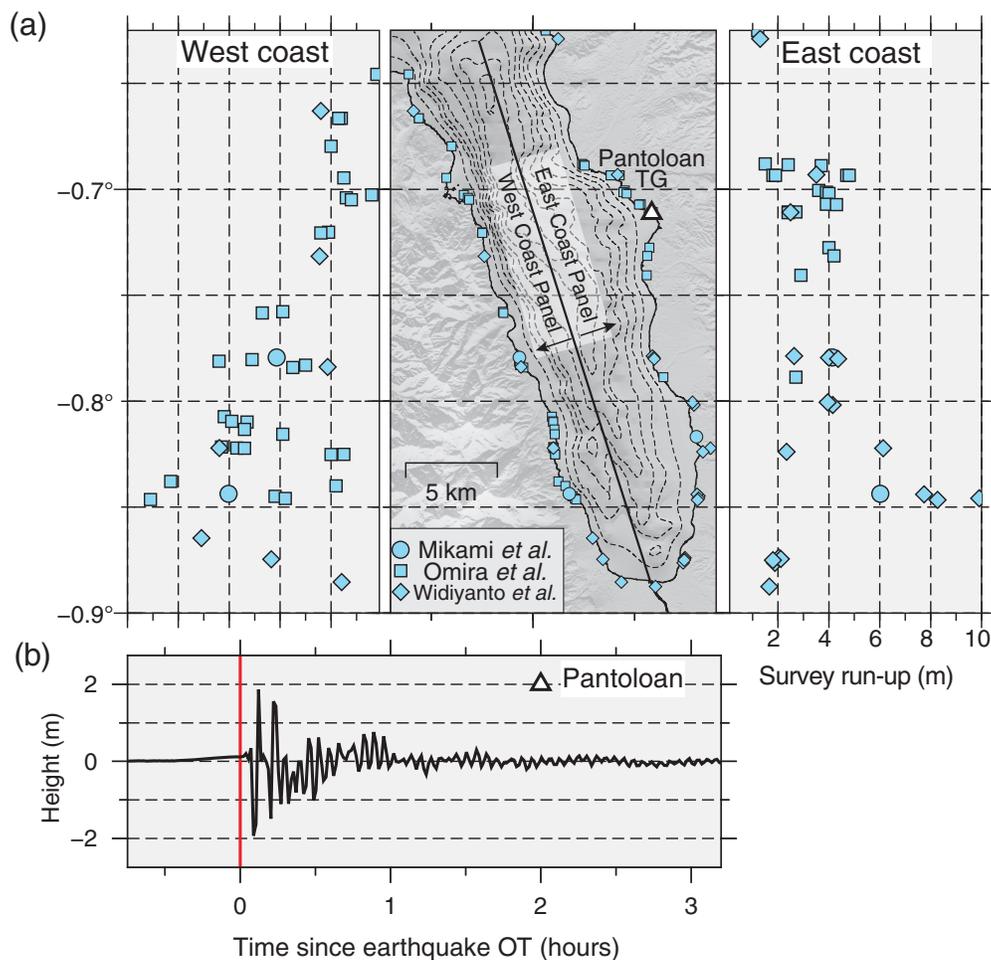
Figure 2. Observational tsunami data set for the Palu earthquake and tsunami. (a) Post-tsunami field survey results focusing on run-up compiled from Mikami et al. (2019), Omira et al. (2019), and Widiyanto et al. (2019) as blue circles, squares, and diamonds, respectively. Survey and future model results are separated onto west and east coast panels as delineated by the straight black line through the center of Palu Bay. Pantoloan tide gauge is marked with a white triangle. Palu City is located at the southern extent of Palu Bay. (b) De-tided tide gauge recording from Pantoloan tide gauge for the 40 min prior to and 3 hr after the earthquake. Earthquake origin time is marked by a red line. OT, origin time; TG, tide gauge. The color version of this figure is available only in the electronic edition.

allows for more complex and bending geometries without subfaults overlapping.

Model A is the simplest and is similar geometry to what has been used in previous studies (Heidarzadeh et al., 2019; Socquet et al., 2019; Song et al., 2019); the northern and southern traces are connected diagonally through the bay. Model B introduces more complexity and connects both sections through a right-stepping restraining bend perpendicular to the bay. Model C, meanwhile, has two discontinuous faults, the northern initiating fault and the Palu-Koro fault extending along the western coast of the bay (Walpersdorf et al., 1998; Bellier et al., 2001, 2006).

Coseismic source inversion

We invert for slip using a non-negative least-squares inversion algorithm (Melgar and Bock, 2015) and incorporating equally weighted LoS InSAR and optical offsets from satellite imagery. We used a velocity model that is local to central Sulawesi through CRUST1 (Laske et al., 2013). We employ a Tikhonov regularization scheme and restrict the total moment of our solution to match the USGS determined M_w 7.5 magnitude.

through the bay, as well as how the fault connects to the earthquake's hypocenter to the northeast, is unclear. Multiple geologic studies of the regions as well as more recent modeling work have used a range of fault interpretations (Walpersdorf et al., 1998; Bellier et al., 2006; Socquet et al., 2006; Socquet et al., 2019; Song et al., 2019). Because of the uncertainty, we test three model geometries labeled A, B, and C (Fig. 1) all east dipping at 67° to match the focal mechanism. Based on past Global Postioning System surveys, we limit the seismogenic depth to 15 km (Socquet et al., 2006). Each model is discretized using a triangular mesh. We used the 3D finite-element mesher GMSH (Geuzaine and Remacle, 2009). The mean size of the bisector of the triangular subfault patches is 3 km. The use of triangles, rather than rectangular patches,

Landslide identification

Each subaerial landslide feature was inspected using rapidly acquired satellite imagery through the ESRI Earthquake Disaster Response program (ESRI, 2018). We identified the 11 largest landslides and measured the surface area lost and an estimated scarp length. Coastal land loss for all 11 slides is outlined in Figure 3. The satellite timing, landslide scaling, and tsunami model parameters are contained in Table 2. Additional possible landslide events located outside of Palu bay at locations (119.776° E, 0.5317° S), (119.805° E, 0.1499° S), and (119.8181° E, 0.1163° S) are ignored in this study due to a latency between satellite images of over 2 yr.
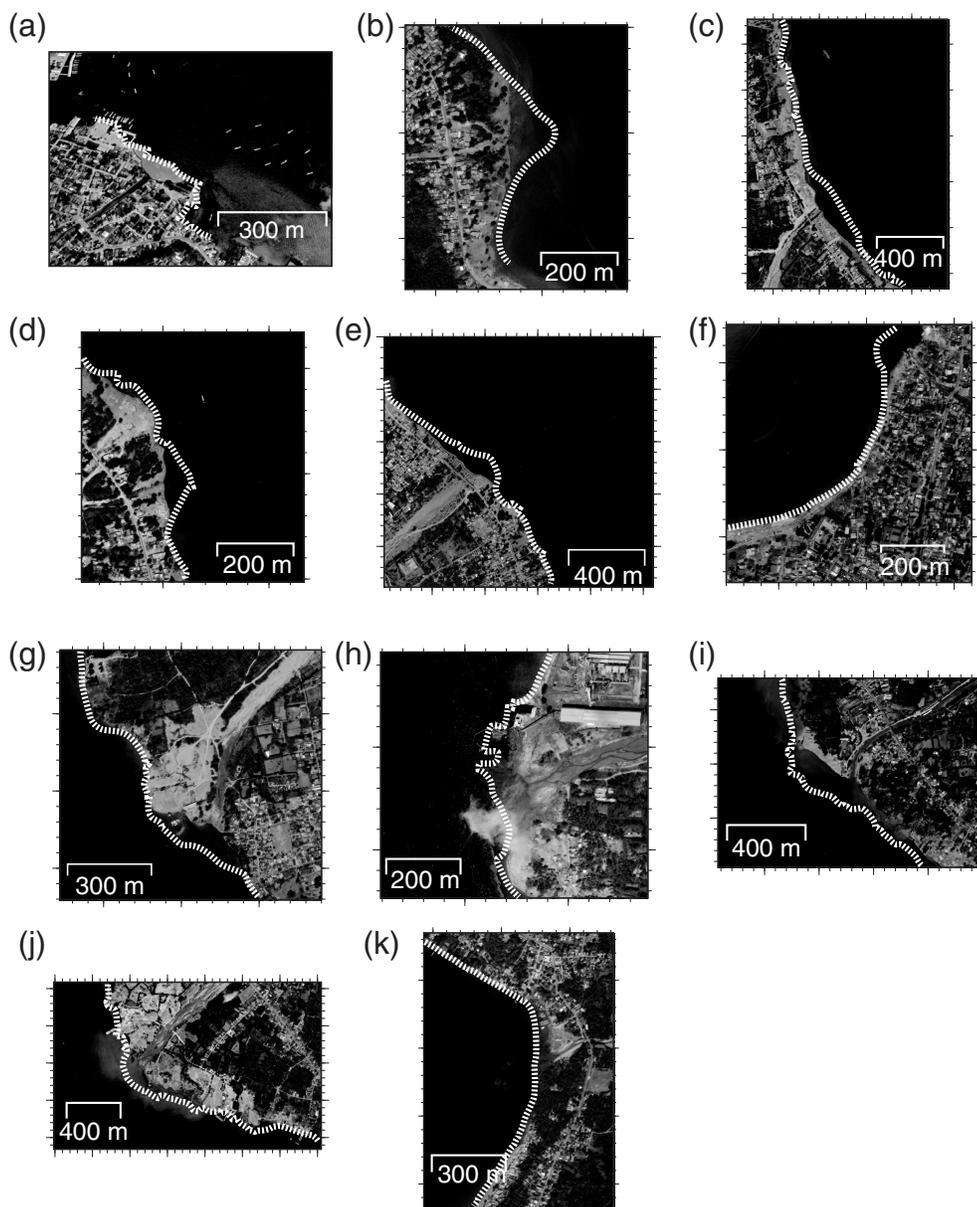
Figure 3. Coastal land loss for all identified landslides. White dashed line indicates pre-earthquake coastline. Time before and after satellite passes is in Table 2, as well as estimated scarp length and area loss. Locations of landslides (a–k) A–K are shown in Figure 6.

compute the tsunamigenic contribution due to the horizontal motion of seafloor topography following the gradient approach in Melgar and Bock (2015) in which

$$\Delta h(x, y) = \Delta z - \Delta x \frac{dh(x, y)}{dx} - \Delta y \frac{dh(x, y)}{dy}. \quad (1)$$

Here, Δh is the vertical deformation of the bathymetry, which is the sum of cosesimic vertical deformation, Δz, as well as the vertical component of lateral motion in the x-, and y-directions, which depends on the gradient of the local bathymetry (Fig. S5). The negative signs are necessary because it is negative gradients (downslope) that are contributing to tsunamigenesis. All models assume an instantaneous deformation. Some recent studies have argued for a potential contribution to tsunami generation from the time kinematic component rupture (Ulrich *et al.*, 2019). However, it has been shown that the large order of magnitude difference between typical earthquake rupture speeds and tsunami propagation speeds means that sources can be treated as instantaneous (Williamson *et al.*, 2019; Riquelme *et al.*, 2020). For the Palu earthquake the short source duration compounded by its super-shear rupture (Bao *et al.*, 2019; Socquet *et al.*, 2019) negates any potential kinematic effects.

We run each model for one hour of propagation time, letting the time step fluctuate to satisfy a preset Courant–Friedrichs–Lewy condition of 0.75 to ensure stability. The model has a moving boundary condition that allows nodes along the coastline to be wetted and dried throughout the propagation. Bottom friction is achieved using a Manning coefficient of 0.025, which is suitable for tsunami propagation through fully submarine channels (Bricker *et al.*, 2015).

Tsunami modeling

We model all tsunami results using the open-source code GeoClaw, which solves the depth-averaged nonlinear shallow-water wave equations in 2D (see LeVeque *et al.*, 2011, and references therein). We initialize all three cosesimic tsunami models by computing the seafloor deformation through the superposition of dislocations related to triangular faults (Comninou and Dundurs, 1975), similar to the Okada equations, which consider dislocations on rectangular faults (Okada, 1985). Because the majority of slip through the bay is expected to contain a strike-slip component, we also

TABLE 2
Subaerial Landslide Coastal Locations and Expected Area Based on Land Changes Between Two Satellite Passes

ID	Longitude (°)	Latitude (°)	Area (m²)	Scarp Length (m)	Amplitude (m)	Before Satellite (yyyy/mm/dd)	After Satellite (yyyy/mm/dd)
A	119.7461	−0.6668	10,972	266	5	2018/09/07	2018/10/01
B	119.7871	−0.755	13,278	260	6	2018/09/26	2018/09/30
C	119.8055	−0.8012	53,824	711	4	2018/09/26	2018/09/30
D	119.8107	−0.8077	10,588	223	4	2018/09/26	2018/10/01
E	119.8228	−0.846	35,826	732	5	2018/08/16	2018/10/01
F	119.8706	−0.8795	15,324	314	4	2018/08/16	2018/10/01
G	119.8627	−0.7896	33,028	530	2	2018/09/26	2018/10/01
H	119.8528	−0.7367	20,788	344	3	2018/09/26	2018/10/01
I	119.845	−0.7021	39,473	374	3	2018/09/26	2018/10/01
J	119.8224	−0.6884	36,507	442	6	2018/09/26	2018/10/01
K	119.8113	−0.6302	14,993	411	5	2016/10/24	2018/10/01

Amplitude is the seafloor displacement from the landslide assuming an instantaneous deformation and scaled to approximate local run-up values.

We fix our bottom friction coefficient as static for all our tsunami models. Although difference coefficients can be used for variable land-use, the difference may not be significant compared to uncertainties in coastal topography. We model the tsunami within the bay using 6 s bathymetry and 0.27 s coastal topography from Badan Informasi Geospasial (BIG). This is the finest scale bathymetry available following the event. We interpolated the bathymetry to the resolution of the coastal data, and to lower the computational cost, we use adaptive mesh refinement. Our coarsest mesh is 10 s and the finest mesh, reserved for modeling points of interest along the coast, is 0.27 s with three levels of refinement in between.

Run-up is calculated by querying points at the 1 arcs spatial scale up to the 15 m elevation contour using the BIG 0.27 s topography digital elevation model (DEM). To compare with published run-up observations, we use 500 m sized bins along latitude for the eastern and western flanks of the bay. Because of multiple observed run-ups within the same latitude, the survey data set is plotted as is for comparison and is not binned but instead plotted as published in Omira *et al.* (2019), Mikami *et al.* (2019), and Widiyanto *et al.* (2019).

We assess the goodness of fit of the tsunami model to the tide gauge measurement using the normalized root-mean-square misfit (NRMS) method (Heidarzadeh *et al.*, 2016). We interpolate the tide gauge and modeled waveform to the same sample rate and concentrate on the first 10 min of observed and modeled tsunami waveforms to capture both the trough and then crest of the initial wave as well as its delayed arrival. A perfect fit corresponds to a NRMS of 0. All NRMS fits are included in Table 3.

We test the tsunamigenic potential of all eleven landslides by modeling each as static block movements into the bay, forgoing the initial water–soil interaction of a two-phase flow due to significant uncertainties in slide velocity and total volume. This highly simplified approach creates a subsidence–subsidence-shaped dipole offshore in the downslope direction from the identified subaerial landslide. This creates a positive wave in the direction of material deposition (bayward) and a negative wave at the location of excavation (coastal to the collapse) and is similar to the treatment of past landslide tsunamis when data are limited (Okal and Synolakis, 2004; Heidarzadeh and Satake, 2015; Heidarzadeh *et al.*, 2020). We prescribe the diameter of each source is equal to the width of the scarp of the corresponding landslide. The goal of this portion of the analysis is to identify the magnitude of landsliding that would be reasonable to recreate the observed tsunami run-up. Therefore, we scale the maximum amplitude of each seafloor perturbation to best fit the nearby survey measurements, recording our model parameters in Table 2. Because we use a nondispersive tsunami model, we focus our fit on run-up values local to each source and acknowledge the limitations that this places when modeling the tsunami across the bay to the tide gauge.

Results
Coseismic tsunami component
Our three finite-fault models (Fig. 4) reveal a consistent behavior despite slight differences in fault geometry through Palu Bay. Slip northeast of the bay, where the earthquake initiated is dominantly strike-slip and shallow (<5 km). As the fault

TABLE 3
Normalized Root Mean Square Misfit (NRMS) Values for Each Tsunami Model

Model	NRMS
Model A	1.019
Model B	1.573
Model C	0.925
Model C + landslides	0.964
Model C + landslides + submarine	0.897

Misfit is calculated for the first 10 min of tsunami propagation.

enters the bay, slip diminishes before resuming south of Palu City. Slip in this southern section extends down to 15 km with a narrow yet continuous band of slip in exceedance of 5 m at a depth of about 10 km. Along the releasing bend south of Palu City, normal faulting is also observed. Our coseismic model fits the north–south offsets of the optical data set well but does underestimate LoS deformation farther from the fault trace (Figs. S2–S4). The region with the greatest vertical seafloor deformation for all models is in the southern part of Palu Bay, near Palu City. All models show an initial subsidence ranging between 2.5 and 3.2 m. Although slip does occur within the bay in some of our models, it is constrained to strike-slip motion that is largely in the southern part of the bay. Although horizontal motion does have the potential to generate tsunami by displacing seafloor topography, in this case, the areas of greatest lateral motion occur in a part of the bay that is relatively low gradient and therefore does not produce large vertical offsets.

Because of the diminished slip within the bay and its strike-slip nature, the tsunamigenic potential of all coseismic finite-fault models is low. When compared to the observed run-up in Figure 5a, the seismically generated tsunami largely underestimates the observations throughout the bay. The only area where moderate (~2 m) run-up is modeled is along the southern coastline near Palu City, where run-ups largely agree with measured values from Widiyanto *et al.* (2019). Here the coseismic component of the tsunami is likely the driving mechanism for coastal damage. North of the city, the tsunami's impact is greatly diminished. At the Pantoloan tide gauge (Fig. 5b) the model fails to recreate both the large trough to crest amplitude and the arrival time.

Indubitably a coseismic component to the tsunami must exist, and yet all three models have similar seafloor deformation (Fig. S6). For further exploration of additional sources, we continue using model C as a baseline for the coseismic tsunamigenic behavior. We favor this model because it includes the Palu-Koro fault as it extends through the bay, the trace of which previous studies (Walpersdorf *et al.*, 1998; Bellier *et al.*,
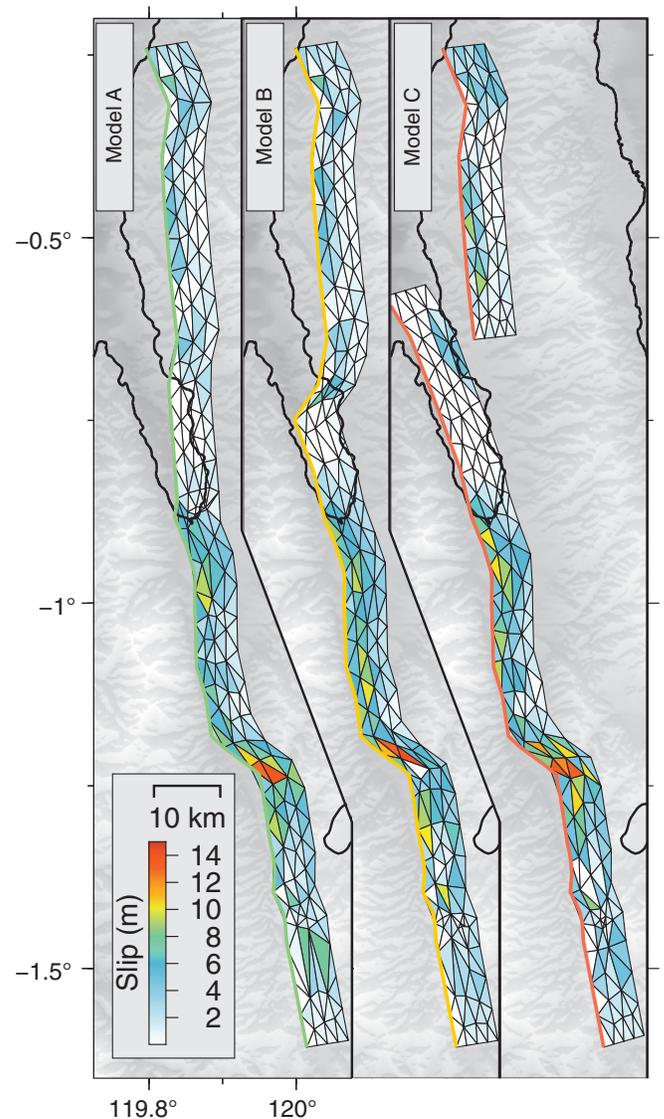

Figure 4. Finite-fault coseismic slip distributions for all three models (A, B, and C) using interferometric synthetic aperture radar (InSAR) and optical offset data. The color version of this figure is available only in the electronic edition.

2001) have confirmed. The possibility of the fault running north–south through the bay, rather than bending, is also corroborated by recent bathymetric surveying (Frederik *et al.*, 2019). Meanwhile, models A and B assume a connection to secondary faults that have not been tectonically validated. The tsunami waveform from model C also has the lowest NRMS (Table 3).

Landslide tsunami component

With the addition of contemporaneous landslides at the locations that we identified as potential sources, we are able to fit the observed run-up (Fig. 6). These landslide sources, which behave as small, dispersive, nearly point sources, match the
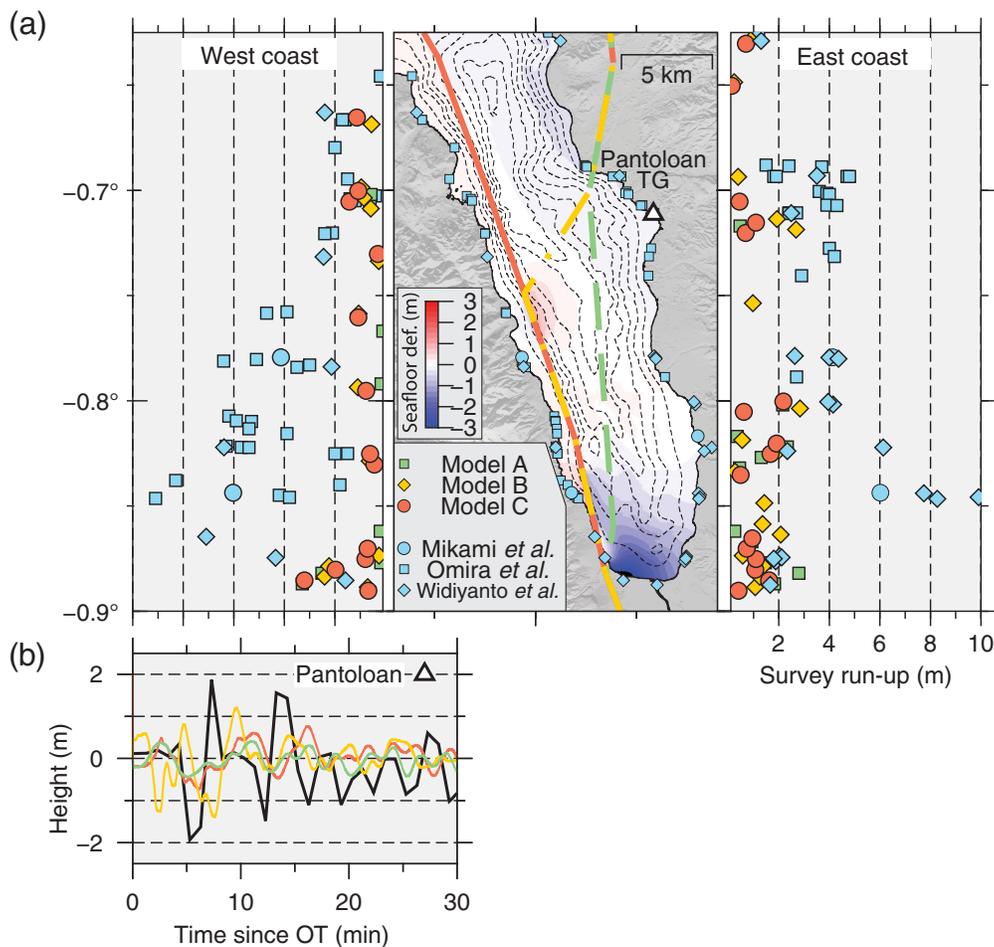
Figure 5. (a) Comparison of observed run-up (blue symbols) at coastal locations to modeled run-up (green, yellow, and red squares, diamonds, and circles, respectively) for models A, B, and C. Fault traces for each of the three models are included in map view. Palu Bay is shaded indicating the coseismic seafloor deformation from model C. Seafloor deformation for all models is in Figure S6. (b) Tsunami models (green, yellow, and red) against recording at Pantoloan tide gauge (black line). The color version of this figure is available only in the electronic edition.

the tide gauge as our starting point, we trace the potential travel time of the tsunami out into the rest of the bay to provide a baseline for the arrival of potential large submarine or coastal landslides. By assuming a reciprocity principle between source and receiver (Hossen et al., 2015), we identify regions where an additional tsunami component could nucleate and reach the tide gauge at the same time as the arrival of the first large negative wave. We follow the methods of Satake (1988) and Gusman et al. (2017) to trace the tsunami for 10 min of tsunami propagation using the highest resolution of our bathymetric model (0.27 s). We use a tracing time step of 5 s and test for initial paths between 0° and 360° at intervals of 0.1°. We find that a large source originating within the port of Pantoloan would arrive at the tide gauge in under 2 min, a source from directly across the bay would arrive within 4 min, and a source located near Palu City would take up to 10 min to reach the gauge.

Assuming all tsunami sources occurred during the earthquake rupture, the areas where a tsunami source would best explain the tide gauge's arrival time are to the north of Pantoloan, near Dongala, and south, between Pantoloan and Palu City (Fig. 6). By incorporating one additional offshore tsunami source, we are able to recover the arrival time and most of the amplitude at the tide gauge, as well as the field survey run-up (Fig. 6). We scale the size and amplitude of the source to match the wavelength and peak amplitude of the tide gauge signal. Although the coastal run-up is best described by small, high-amplitude sources, the longer wavelength signal at the tide gauge fits best with a wider, offshore source.

high spatial variability in run-ups along the eastern and western coastlines. For example, on the western coast of Palu bay 8+ m run-ups are recreated without creating equally large yet unobserved run-ups on the eastern coast at the same latitudes. However, although the survey data are largely recreated, an inconsistency remains: the inclusion of subaerial sources does not sufficiently improve the waveform fit at the Pantoloan tide gauge. Because of the small and dispersive nature of the potential landslides, they do not produce waves that effectively propagate across the bay, nor with the 6-min period observed at the tide gauge.

To explain this last piece of the tsunami observations, we hypothesize an additional submarine landslide component the locations and extent of which can be constrained from a raytracing analysis (Gusman et al., 2017) of the travel time from the gauge into the bay (Fig. 7). Using the location of

We prefer the inclusion of the southern submarine landslide source because it occurs in an area that has steep bathymetry, is near two coastal landslide sites, and coincides with the highest observed run-ups within Palu Bay. A potential source in the
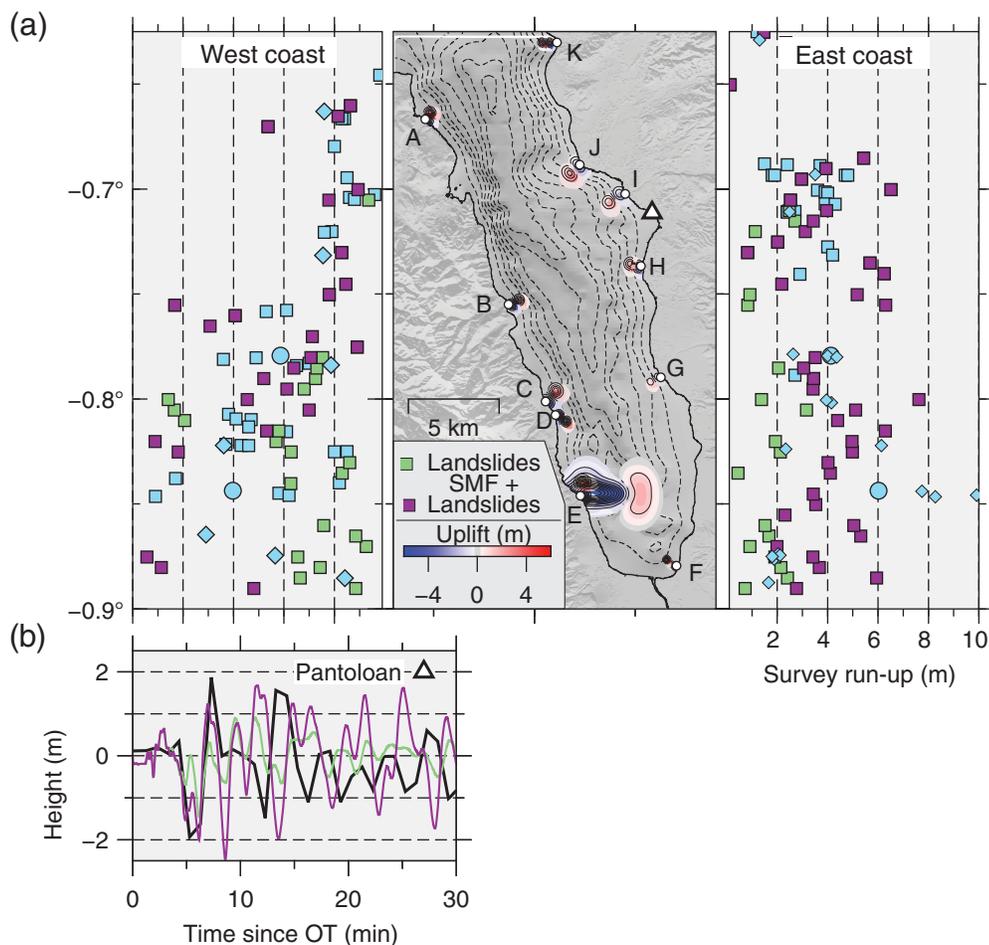
Figure 6. (a) Comparison of observed run-up (blue symbols) to modeled run-ups (green bars) for a combined coastal landslide and model C source and with the addition of a hypothesized submarine mass failure (SMF) and landslide component (purple). Shaded deformation within the map view shows the initial vertical seafloor offsets from each landslide source. Tide gauge indicated by a white triangle and the locations of all landslides are labeled A–K and denoted by a white dot. (b) Comparison of observed waveform (black) to models (green and purple) for the first 30 min following the start of the earthquake. The color version of this figure is available only in the electronic edition.

Discussion

With all three tsunamigenic components: the modest coseismic deformation, the subaerial landslides, and the inclusion of a deeper submarine slump, the signal at the tide gauge, and the survey run-ups are largely recovered. One small difference, however, is that the final synthetic tide gauge model has higher-frequency waves, due to coastal landslide sources arriving prior to the main tsunamigenic component at 5 min. These cannot be seen in the observed record, possibly due to the low 60 s sampling rate. Though without the inclusion of these landslide sources, the run-up in the near field is largely underestimated. The timing of these early high-frequency waves are corroborated with video footage from the inside of the bay and close to the tide gauge (Carvajal *et al.*, 2019).

The inclusion of the additional submarine landsliding component is the last piece to the puzzle explaining the size of the tsunami. However, although the coastal landslides are visible through rapidly acquired satellite imagery following the event, it is much harder to determine the verac-
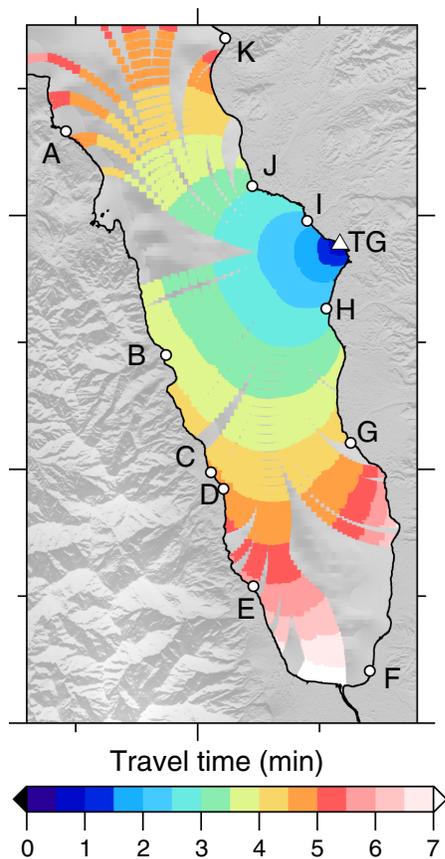
southern portion of Palu Bay would also help increase the fit to tsunami run-up values on the southeast coast (near −0.85°), which exceed 6 m. This area does not have an identified coastal landslide that may contribute to tsunami run-up. Our inferred southern submarine source is near the location of a possibly identified seafloor slump (Takagi *et al.*, 2019) and is corroborated by Widiyanto *et al.* (2019), which also supports the idea of a submarine landslide in the southern portion of Palu Bay. Possible source locations north of Pantoloan, although arriving at the tide gauge at the correct time and as advocated for in Pakoksung *et al.* (2019), would contradict the comparatively low (2 m to the north vs. 6 m to the south) observed run-up values from Omira *et al.* (2019). A source to the southeast, although also plausible, would occur in an area with a much gentler bathymetric slope.

ity of submarine sources. We postulate that the large number of mass failures does not simply stop at the water line but rather would continue along steeper submarine slopes within the bay. Although detailed seafloor surveys following the Palu event exist (Frederik *et al.*, 2019), the resolution is limited to locations within the bay at depths of greater than 50 m, which largely excludes the coast near the subaerial landslides.

In complement to seafloor surveys, raytracing helps to narrow down possible tsunami source locations that would arrive at the local tide gauge with the appropriate timing. This requires high-resolution bathymetry and coastal DEMs as the tsunami's velocity is dependent on the water depth. Because Palu bay is so narrow, only 5 km across, changes in water depth between coarser and finer models can greatly

Figure 7. Tsunami raytracing results within Palu Bay for a source located at the Pantoloan tide gauge. Landslide sources from Table 2 are marked as A–K with white dots along the coast. Color scale ranges from 0 to 7 min at 30 s increments. The color version of this figure is available only in the electronic edition.

affect the raytracing solution. In this study we use the finest scale bathymetry and coastal DEMs available through BIG. The higher resolution bathymetry recovers features within the bay that are not seen in coarser models, which affects tsunami propagation for both modeling purposes as well as raytracing.

The results of raytracing allow us to exclude scenarios in which coseismic slip on submarine faults generates a tsunami with too early of an arrival time. Many postulated fault geometries with moderate coseismic slip, particularly through the use of a restraining bend or other exotic geometries (Heidarzadeh *et al.*, 2019; Song *et al.*, 2019; Ulrich *et al.*, 2019) to promote tsunamigenic vertical deformation on the seafloor occur within the area described by the raytracing exercise as too close to the tide gauge to have the correct tsunami arrival time. This limits a coseismic-only generated tsunami to the northern and southern portions of the bay. Although it could be argued that the timing on the tide gauge is perhaps erroneous or inaccurate (Heidarzadeh *et al.*, 2019), video footage local to Pantoloan confirms the main tsunami arrival time

(Carvajal *et al.*, 2019). Raytracing also allows us to narrow down a potential large submarine component to a few candidate locations. Analysis of coastal run-up provided through field surveys allows us to further narrow down the locations of possible tsunami sources. Through raytracing, we identify that a hypothetical submarine mass failure would be ideally placed either north, toward the opening of Palu Bay, or toward the south, near Palu City. Our prioritization of southern Palu Bay tsunami sources fits well with the extreme local run-up. Large tsunami sources, either coseismically or through landsliding, located at the entrance to or outside of Palu Bay simply contradict the results of field surveys that show little damage and low run-ups at those localities (Omira *et al.*, 2019).

There are multiple unknowns that need to be addressed when handling the landslide portion of the study. Although we can identify the locations of potential events using rapid satellite imagery, we cannot constrain the timing of landsliding events down to the minute scale. We treat all landslide sources as occurring near instantaneously or shortly after to the earthquake rupture, likely triggered due to seismic shaking; however, it is possible that one or multiple landslides are delayed by over a minute. Although this does not affect the run-up observed along local coastlines, it could affect the timing of the tsunami recording at the tide gauge. This is particularly true of the two landslides (I and H) that are closest to the tide gauge. Information about the velocity of the landslides as they enter the bay, which influences the tsunami potential, is also unknown. Here we assume an instantaneous deformation, following accounts recorded in Takagi *et al.* (2019) of a near-instant arrival of a landslide in the southeast portion of the bay.

The locations that we identified as potential landslides sites are corroborated with other published landslide-focused work. Takagi *et al.* (2019) conducted a bathymetric survey in the southwest portion of Palu Bay, mapping a mass wasting event that we identified as landslide E. Although they do not model the landslide in conjunction with other potential sources, they infer that this source is what may have caused the instantaneous tsunami reported by eyewitnesses along the immediate surroundings. Pakoksung *et al.* (2019) hypothesize multiple submarine sources, one of which is located in a similar position in the southern part of Palu Bay as ours, as well as three sources north of the bay. They also model small landslides based on eyewitness reports. Widiyanto *et al.* (2019) also support the possibility of a southern fully submarine landslide.

The Palu tsunami represents a complex tsunamigenic scenario where the earthquake was a contributor but not the primary cause of the tsunami. Instead the earthquake likely triggered the landsliding that produced the damaging waves. Bao *et al.* (2019) and Socquet *et al.* (2019) both conclude in separate studies that the earthquake was likely a supershear rupture. Such ruptures can generate stronger than average

shaking that could act as the impetus for the large number and wide spatial distribution of mass wasting throughout the bay. Supershear ruptures are thought to be more prevalent along strike-slip faults. Although these are traditionally less tsunamigenic environments, the Palu tsunami proves that exceptions to this assumption do occur. Understanding these exceptional events is important not just for the region of Sulawesi but for other places where there are offshore strike-slip faults such as California, Greece, Turkey, Western Canada, and Alaska. As postulated (Mai, 2019), other strike-slip faults such as the San Andreas and North Anatolian faults intersect bodies of water and may be susceptible to similar tsunami hazards as Palu Bay. Similar events as this are also a potential threat in environments where nonseismic landslides are already common and are paired with an expected future seismic hazard such as parts of the U.S. Pacific Northwest.

Conclusion

We conclude that the coseismic source contributes primarily to the large tsunami near Palu City in the south of Palu Bay. The remainder of the bay experiences a tsunami that was devastating primarily because of subaerial and submarine landsliding. The likelihood landslide tsunamis may be enhanced by the elevated shaking associated with super-shear ruptures as was likely the case here (Bao *et al.*, 2019; Socquet *et al.*, 2019). Landslide-induced tsunamis, particularly in narrow bays near large population centers, pose a difficult challenge for tsunami hazard assessment. Our model, as well as field observations, shows a devastating tsunami that inundated nearly all coasts in the bay within 5 min. Even with state-of-the-art warning systems, it would be highly challenging to give sufficient lead-time to prevent a catastrophe as occurred during the Palu event. Nonetheless, the identification and inclusion of future landslide-induced tsunami sources should continue to be a priority in regional tsunami hazard assessments.

Data and Resources

Additional figures showing geodetic inversion model fits, modeled seafloor deformation, and landslide locations are available in the supplemental material. Bathymetric data were accessed from Badan Informasi Geospasial (BIG) at http://tides.big.go.id/ (last accessed January 2020). Satellite imagery is open access and was acquired through Google Earth. Figures were made using Generic Mapping Tools (Wessel *et al.*, 2013). Advanced Land Observing Satellite-2 (ALOS-2) data were provided by the Japan Aerospace Exploration Agency (JAXA) under investigation 1148. The MudPy source inversion code can be found at https://github.com/dmelgarm/mudpy/ (last accessed December 2019). The GeoClaw tsunami modeling code can be obtained from https://www.clawpack.org/ (last accessed December 2019). The tsunami record, unwrapped interferometric synthetic aperture radar (InSAR) scenes, and visible imagery are available from the corresponding author upon request. The authors thank A. R. Gusman for access to the tsunami raytracing code; it can be found at https://github.com/adityagusman/tsunami-raytracing (last accessed December 2019).

References

Arikawa, T., A. Muhari, Y. Okumura, Y. Dohi, B. Afriyanto, K. A. Sujatmiko, and F. Imamura (2018). Coastal subsidence induced several tsunamis during the 2018 Sulawesi earthquake, *J. Disast. Res.* **13,** 1–3.

Bao, H., J. P. Ampuero, L. Meng, E. J. Fielding, C. Liang, C. W. D. Milliner, T. Feng, and H. Huang (2019). Early and persistent supershear rupture of the 2018 magnitude 7.5 Palu earthquake, *Nat. Geosci.* **12,** 200–205, doi: 10.1038/s41561-018-0297-z

Bellier, O., M. Sébrier, D. Seward, T. Beaudouin, M. Villeneuve, and E. Putranto (2006). Fission track and fault kinematics analyses for new insight into the Late Cenozoic tectonic regime changes in West-Central Sulawesi (Indonesia), *Tectonophysics* **413,** nos. 3/4, 201–220.

Bellier, O., L. Siame, T. Beaudouin, M. Villeneuve, and R. Braucher (2001). High slip rate for a low seismicity along the Palu-Koro active fault in Central Sulawesi (Indonesia), *Terra Nova* **13,** no. 6, 463–470, doi: 10.1046/j.1365-3121.2001.00382.x.

Bricker, J. D., S. Gibson, H. Takagi, and F. Imamura (2015). On the need for larger Manning's roughness coefficients in depth-integrated tsunami inundation models, *Coast. Eng. J.* **57,** no. 02, 1550005.

Carvajal, M., C. Araya-Cornejo, I. Sepúlveda, D. Melnick, and J. S. Haase (2019). Nearly-instantaneous tsunamis following the M_w 7.5 2018 Palu earthquake, *Geophys. Res. Lett.* **46,** 5117–5126, doi: 10.1029/2019GL082578.

Chen, A. C., and H. A. Zebker (2013). Reducing ionospheric effects in InSAR data using accurate coregistration, *IEEE Trans. Geosci. Remote Sens.* **52,** no. 1, 60–70.

Comninou, M., and J. Dundurs (1975). The angular dislocation in a half space, *J. Elast.* **5,** nos. 3/4, 203–216.

Debella-Gilo, M., and A. Kääb (2011). Sub-pixel precision image matching for measuring surface displacements on mass movements using normalized cross-correlation, *Remote Sens. Environ.* **115,** no. 1, 130–142.

ESRI (2018). *Disaster Response Program*, available at https://www.esri.com/en-us/disaster-response/disasters/earthquakes (last accessed November 2019).

Frederik, M. C., R. Adhitama, N. D. Hananto, S. Sahabuddin, M. Irfan, O. Moefti, D. B. Putra, and B. F. Riyalda (2019). First results of a bathymetric survey of Palu Bay, Central Sulawesi, Indonesia following the Tsunamigenic Earthquake of 28 September 2018, *Pure Appl. Geophys.* **176,** no. 8, 3277–3290.

Geuzaine, C., and J. F. Remacle (2009). GMSH: A 3-D finite element mesh generator with built-in pre- and post-processing facilities, *Int. J. Numer. Methods Eng.* **79,** no. 11, 1309–1331.

Gusman, A. R., K. Satake, M. Shinohara, S. I. Sakai, and Y. Tanioka (2017). Fault slip distribution of the 2016 Fukushima earthquake estimated from tsunami waveforms, *Pure Appl. Geophys.* **174,** no. 8, 2925–2943.

Heidarzadeh, M., and K. Satake (2015). Source properties of the 1998 July 17 Papua New Guinea tsunami based on tide gauge records. *Geophys. J. Int.* **202,** no. 1, 361–369.

Heidarzadeh, M., T. Ishibe, O. Sandanbata, A. Muhari, and A. B. Wijanarto (2020). Numerical modeling of the subaerial landslide source of the 22 December 2018 Anak Krakatoa volcanic tsunami, Indonesia, *Ocean Eng.* **195,** 106733.

Heidarzadeh, M., A. Muhari, and A. B. Wijanarto (2019). Insights on the source of the 28 September 2018 Sulawesi Tsunami, Indonesia based on spectral analyses and numerical simulations, *Pure Appl. Geophys.* **176,** no. 1, 25–43, doi: 10.1007/s00024-018-2065-9.

Heidarzadeh, M., S. Murotani, K. Satake, T. Ishibe, and A. R. Gusman (2016). Source model of the 16 September 2015 Illapel, Chile, M_w 8.4 earthquake based on teleseismic and tsunami data, *Geophys. Res. Lett.* **43,** no. 2, 643–650.

Hornbach, M. J., N. Braudy, R. W. Briggs, M. H. Cormier, M. B. Davis, J. B. Diebold, N. Dieudonne, R. Douilly, C. Frohlich, S. P. Gulick, et al. (2010). High tsunami frequency as a result of combined strike-slip faulting and coastal landslides, *Nat. Geosci.* **3,** no. 11, 783–788, doi: 10.1038/ngeo975.

Hossen, M. J., P. R. Cummins, S. G. Roberts, and S. Allgeyer (2015). Time reversal imaging of the tsunami source, *Pure Appl. Geophys.* **172,** nos. 3/4, 969–984.

Imamura, F., C. E. Synolakis, E. Gica, V. Titov, E. Listanco, and H. J. Lee (1995). Field survey of the 1994 Mindoro Island, Philippines tsunami, *Pure Appl. Geophys.* **144,** no. 3–4, 875–890.

Laske, G., G. Masters, Z. Ma, and M. Pasyanos (2013). Update on CRUST1.0—A 1-degree global model of Earth's crust, *Geophys. Res. Abstr,* EGU General Assembly, Vienna, Austria, Vol. 15, p. 2658.

LeVeque, R. J., D. L. George, and M. J. Berger (2011). Tsunami modelling with adaptively refined finite volume methods, *Acta Numer.* **20,** 211–289.

Mai, P. M. (2019). Supershear tsunami disaster, *Nat. Geosci.* **12,** no. 3, 150–151, doi: 10.1038/s41561-019-0308-8.

Melgar, D., and Y. Bock (2015). Kinematic earthquake source inversion and tsunami runup prediction with regional geophysical data, *J. Geophys. Res.* **120,** no. 5, 3324–3349.

Mikami, T., T. Shibayama, M. Esteban, T. Takabatake, R. Nakamura, Y. Nishida, H. Achiari, A. G. Marzuki, M. F. H. Marzuki, J. Stolle, et al. (2019). Field survey of the 2018 Sulawesi tsunami: inundation and run-up heights and damage to coastal communities, *Pure Appl. Geophys.* **176,** no. 8, 3291–3304.

Mori, N., T. Takahashi, T. Yasuda, and H. Yanagisawa (2011). Survey of 2011 Tohoku earthquake tsunami inundation and run-up, *Geophys. Res. Lett.* **38,** no. 18, 6–11, doi: 10.1029/2011GL049210.

National Geophysical Data Center (NGDC) (2018). Sulawesi, Indonesia, Earthquake and Tsunami, September 28, 2018, available at https://www.ngdc.noaa.gov/hazard/28sep2018.html (last accessed January 2020).

Okada, Y. (1985). Surface deformation due to shear and tensile faults in a half-space, *Bull. Seismol. Soc. Am.* **75,** no. 4, 1135–1154.

Okal, E. A., and C. E. Synolakis (2004). Source discriminants for near-field tsunamis, *Geophys. J. Int.* **158,** no. 3, 899–912.

Omira, R., G. G. Dogan, R. Hidayat, S. Husrin, G. Prasetya, A. Annunziato, C. Proietti, P. Probst, M. A. Paparo, M. Wronna, et al. (2019). The September 28th, 2018, Tsunami in Palu-Sulawesi, Indonesia: A post-event field survey, *Pure Appl. Geophys.* **176,** no. 4, 1379–1395, doi: 10.1007/s00024-019-02145-z.

Pakoksung, K., A. Suppasri, F. Imamura, C. Athanasius, A. Omang, and A. Muhari (2019). Simulation of the submarine landslide Tsunami on 28 September 2018 in Palu Bay, Sulawesi Island, Indonesia, using a two-layer model, *Pure Appl. Geophys.* **176,** 3323–3350.

Paulik, R., A. Gusman, J. H. Williams, G. M. Pratama, S. L. Lin, A. Prawirabhakti, K. Sulendra, M. Y. Zachari, Z. E. D. Fortuna, N. B. P. Layuk, et al. (2019). Tsunami hazard and built environment damage observations from Palu City after the September 28 2018 Sulawesi earthquake and tsunami, *Pure Appl. Geophys.* **176,** no. 8, 3305–3321.

Planet Team (2018). *Planet Application Program Interface: In Space for Life on Earth*, San Francisco, California.

Putra, P. S., A. Aswan, K. A. Maryunani, E. Yulianto, and W. Kongko (2019). Field survey of the 2018 Sulawesi tsunami deposits, *Pure Appl. Geophys.* **176,** 2203–2213.

Riquelme, S., H. Schwarze, M. Fuentes, and J. Campos (2020). Near field effects of earthquake rupture velocity into tsunami run-up heights, *J. Geophys. Res.* **125,** no. 6, e2019JB018946.

Sandwell, D., R. Mellors, X. Tong, M. Wei, and P. Wessel (2011). GMTSAR: An InSAR processing system based on Generic Mapping Tools, *Scripps Institution of Oceanography Technical Rept.*, San Diego, California.

Sassa, S., and T. Takagawa (2019). Liquefied gravity flow-induced tsunami: First evidence and comparison from the 2018 Indonesia Sulawesi earthquake and tsunami disasters, *Landslides* **16,** no. 1, 195–200.

Satake, K. (1988). Effects of bathymetry on tsunami propagation: Application of ray tracing to tsunamis, *Pure Appl. Geophys.* **126,** no. 1, 27–36.

Socquet, A., J. Hollingsworth, E. Pathier, and M. Bouchon (2019). Evidence of supershear during the 2018 magnitude 7.5 Palu earthquake from space geodesy, *Nat. Geosci.* **12,** 192–199, doi: 10.1038/s41561-018-0296-0.

Socquet, A., W. Simons, C. Vigny, R. McCaffrey, C. Subarya, D. Sarsito, B. Ambrosius, and W. Spakman (2006). Microblock rotations and fault coupling in SE Asia triple junction (Sulawesi, Indonesia) from GPS and earthquake slip vector data. *J. Geophys. Res.* **111,** no. 8, B08409, doi: 10.1029/2005JB003963.

Song, X., Y. Zhang, X. Shan, Y. Liu, W. Gong, and C. Qu (2019). Geodetic observations of the 2018 M_w 7.5 Sulawesi earthquake and its implications for the kinematics of the Palu fault, *Geophys. Res. Lett.* **46,** no. 8, 4212–4220, doi: 10.1029/2019GL082045.

Syamsidik, Benazir, M. Umar, G. Margaglio, and A. Fitrayansyah (2019). Post-tsunami survey of the 28 September 2018 tsunami near Palu Bay in Central Sulawesi, Indonesia: Impacts and challenges to coastal communities, *Int. J. Disaster Risk Reduction* **38,** 101229, doi: 10.1016/j.ijdrr.2019.101229.

Takagi, R., N. Uchida, T. Nakayama, R. Azuma, A. Ishigami, T. Okada, T. Nakamura, and K. Shiomi (2019). Estimation of the orientations of the S-net cabled ocean-bottom sensors, *Seismol. Res. Lett.* **90,** 2175–2187, doi: 10.1785/0220190093.

Ulrich, T., S. Vater, E. H. Madden, J. Behrens, Y. van Dinther, I. van Zelst, E. J. Fielding, C. Liang, and A. A. Gabriel (2019). Coupled, physics-based modeling reveals earthquake displacements are

critical to the 2018 Palu, Sulawesi tsunami, *Pure Appl. Geophys.* **176,** 4069–4109.

U.S. Geologic Survey (USGS) (2018). M 7.5 - 70km N of Palu, Indonesia, available at https://earthquake.usgs.gov/earthquakes/eventpage/us1000h3p4/executive (last accessed January 2020).

Walpersdorf, A., C. Vigny, C. Subarya, and P. Manurung (1998). Monitoring of the Palu-Koro fault (Sulawesi) by GPS, *Geophys. Res. Lett.* **25,** no. 13, 2313–2316, doi: 10.1029/98GL01799.

Watkinson, I. M., and R. Hall (2017). Fault systems of the eastern Indonesian triple junction: evaluation of quaternary activity and implications for seismic hazards, *Geol. Soc. Lond. Spec. Publ.* **441,** no. 1, 71–120, doi: 10.1144/SP441.8.

Wessel, P., W. H. Smith, R. Scharroo, J. Luis, and F. Wobbe (2013). Generic mapping tools: improved version released, *Eos Trans. AGU* **94,** no. 45, 409–410.

Widiyanto, W., P. B. Santoso, S. C. Hsiao, and R. T. Imananta (2019). Post-event field survey of 28 September 2018 Sulawesi earthquake and tsunami, *Nat. Hazards Earth Syst. Sci. Discuss.* **1,** 1–23.

Williamson, A., D. Melgar, and D. Rim (2019). The effect of earthquake kinematics on tsunami propagation, *J. Geophys. Res.* **124,** 11,639–11,650.